GEOPHYSICS®

Bayesian facies inversion on a partially dolomitized isolated carbonate platform. A case study from Central Luconia province, Malaysia.

Journal:	*Geophysics*
Manuscript ID	GEO-2020-0351.R2
Manuscript Type:	Case Histories
Keywords:	inversion, facies, carbonate, AVO/AVA, geology
Manuscript Focus Area:	Case Histories, Reservoir Geophysics

Bayesian facies inversion on a partially dolomitized isolated carbonate platform. A case study from Central Luconia province, Malaysia

George Ghon[1*], Dario Grana[2], Eugene C. Rankey[3], Gregor T. Baechle[4], Florian Bleibinhaus[1], Xiaozheng Lang[5], Leandro Passos de Figueiredo[5], and Michael C. Poppelreiter[6]

[1]*Chair of Applied Geophysics, Montanuniversitaet Leoben. Email: georgeghon@gmail.com*

[2]*Department of Geology and Geophysics, University of Wyoming.*

[3]*Kansas Interdisciplinary Carbonates Consortium, University of Kansas.*

[4]*Repsol E & P, Houston.*

[5]*Physics Department, Federal University of Santa Catarina, Florianópolis, Brazil and LTrace Geophysical Solutions, Florianópolis, Brazil.*

[6]*Shell Kuwait E & P and SEACaRL, Universiti Teknologi Petronas, Seri Iskander, Malaysia.*

**Presently: Earth Science Analytics, Stavanger, Norway*

ABSTRACT

We present a case study of geophysical reservoir characterization where we use elastic inversion and probabilistic prediction to estimate nine carbonate lithofacies and the associated porosity distribution. The study focuses on an isolated carbonate platform of middle Miocene age, offshore Sarawak in Malaysia that has been partly dolomitized – a process that increased porosity and permeability of the prolific gas reservoir. The nine lithofacies are defined from one reference core and include a range of lithologies and pore types, covering limestone and dolomitized limestone, each with vuggy varieties, as well as sucrosic and crystalline dolomites with intercrystalline porosity, and also argillaceous limestones and shales. To predict lithofacies and porosity from geophysical data, we adopt a probabilistic algorithm that employs Bayesian theory with an analytical solution for conditional means and covariances of posterior probabilities, assuming a Gaussian mixture model. The inversion is a two-step process, first solving for elastic model parameters P- and S-wave velocities and density from two partial seismic stacks. Subsequently, lithofacies and porosity are predicted from the elastic parameters in the borehole and across a 2-D inline. The final result is a model that consists of the pointwise posterior distributions of facies and porosity at each location where seismic data are available. The facies posterior distribution represents the facies proportions estimated from seismic data, whereas the porosity distribution represents the probability density function at each location. These distributions provide the most likely model and its associated uncertainty for geological interpretations of lithofacies associated with distinct stages of carbonate platform growth.

INTRODUCTION

Mapping spatial facies distributions in carbonate reservoirs from seismic data remains a challenge due to the considerable vertical and horizontal variability, driven by both depositional and diagenetic processes. We present a quantitative workflow for predicting elastic carbonate lithofacies, henceforth termed facies, and porosity from partial stack seismic data in a probabilistic framework utilizing Bayesian inversion. The results can guide the interpretation of geological processes and reservoir zonation. The data for the case history are from of a middle Miocene isolated carbonate platform in Central Luconia province, Sarawak Basin, Malaysia. A prolific gas reservoir was appraised by Shell during the 1970s, and since then has been subject of sedimentological (Epting, 1980), diagenetic (Warrlich et al., 2010), and seismic stratigraphic (Bracco Gartner et al., 2004; Zampetti et al., 2004a and 2004b; Rankey et al., 2019) studies.

The geological analysis (Ghon et al., 2018) is complemented with a Bayesian inversion method that has been applied successfully to invert seismic data for elastic parameters (Buland and Omre, 2003), petrophysical reservoir properties (Grana, 2016), and lithofacies (Grana and Della Rossa, 2010; de Figueiredo et al., 2017; Grana, 2018). Machine learning methods, for example, based on convolutional and recursive neural networks, can also be applied to seismic facies classification, as shown in Zhang et al. (2018), Liu et al. (2018), Grana et al. (2020), Zhou et al. (2020), and Liu et al. (2020). Facies inversion is generally applied to siliciclastic reservoirs (Avseth et al., 2005); however, in carbonates, petroelastic facies characterization has been pursued by introducing a rock physics model that considers a frame flexibility factor γ (Sun, 2000, 2004; Dou et al., 2011; Karimpouli et al., 2013) or combining lithology and pore fill into litho-fluid classes (Zhao et al., 2014).

The carbonates of the platform have been overprinted heavily by diagenetic processes – dissolution, cementation, and dolomitization, each of which affect elastic behavior. Dolomitization describes a mineralogical change from calcitic to dolomitic rock frame, a process that generally increases mineral density, bulk modulus, and seismic velocities. Dolomitization can also increase porosity, decrease bulk density and lower seismic velocities.

Additionally, textural rock properties and pore types have a pronounced effect on elastic characterization (Eberli et al., 2003, Verwer et al., 2008). Microporosity (Baechle et al., 2008a) tends to weaken the rock frame, with the lowest seismic velocities associated with micro pores, features that can contribute more than 80% of the total porosity (Baechle et al., 2009). Vuggy porosity, on the other hand, can have a stabilizing effect on the rock frame, does not weaken the matrix, and maintains elevated sonic velocities (Baechle et al., 2008b).

In this study, to constrain facies prediction, a recent core description is combined with thin-section and plug data, leading to a designation of a total of nine elastic carbonate facies that range from limestone to dolomite (each with vuggy, sucrosic, and crystalline rock fabrics), and also including argillaceous carbonates, and shale. The inversion is performed in 1-D at the well site, first from well logs upscaled at the seismic sampling rate, and, subsequently, from a seismic trace extracted at the well location. Also, a 2-D inline, extracted from two partially stacked seismic volumes also provides a cross section of the carbonate platform and is inverted for elastic parameters, porosity, and facies. The seismic line is inverted for reservoir parameters and reveals the potential of the Bayesian method as quantitative interpretation tool. This work provides a unique application of the Bayesian classification and inversion approach to a complex carbonate reservoir with a large number of lithological facies.

GEOLOGICAL SETTING

The Central Luconia Province, offshore Sarawak, Malaysia, is part of the shallow (<70 m water depth) Sunda Shelf, in the western South China Sea (Figure 1). The Luconia block is a micro-continental unit accreted to the landmass of Borneo in the early Miocene (Hall and Spakman, 2015). The accretion led to regional uplift, an increase in erosion, and copious production of siliciclastic sediment, fed to the shelf via large deltas. The basin has a flexural foreland character, and shows a forebulge (Steuer et al., 2014). A region-wide Red or Middle

Miocene unconformity has been interpreted to represent the impact of compression, and subaerial exposure in Central Luconia around 17 – 18 Ma ago (Steuer et al., 2014). The complex tectonic regime, influenced by the pull of subducting slabs, the rifting and opening of the South China Sea, and the collision of Central Luconia with Borneo led to rotation (Hall and Spakman, 2015). This regional rotation in turn caused a trans-tensional stress regime on the north-western shelf of Borneo, establishing NNE – SSW trending normal faults active during the middle Miocene, thereby forming horsts, which favored growth of isolated carbonate platforms (Koša et al., 2015).

The stratigraphic framework on the Sarawak shelf is subdivided into eight transgressive-regressive cycles, ranging in age from late Eocene to present, and defined by boundaries that form regional angular unconformities (Fui, 1978; Hageman, 1987). The most prolific growth of isolated carbonate platforms in Central Luconia occurred within cycles IV and V. The initiation of Cycle IV is linked to a transgression, the onset of which has been dated by micro fossils as lower NN4 Martini zone, at around the early/middle Miocene boundary, or 15.5 - 16 Ma ago (Lunt and Madon, 2017).

The EX platform, the focus of this study, is one of the isolated carbonate platforms that grew during the middle Miocene on a regional high. Its lower, flat-topped unit has been interpreted as the "build-out" stage of platform development, occurring during Sarawak Cycle IV (Epting, 1980; Zampetti et al., 2004a and 2004b). During deposition of Cycle V, sediment input from the Borneo hinterland increased, as suggested by progradation of the Baram Delta (Lunt and Madon, 2017). During the deposition of the upper part of Cycle V, the EX platform started to retrograde, or "build-in," forming an elongate "pinnacle," which narrowed toward the top, drowned, and eventually was buried by siliciclastics (Figure 2). The EX isolated carbonate platform forms an ellipsoid, up to 10 km x 5 km, with its long axis roughly North-South. An exploration well (EX-1) in 1971 penetrated a 400 m thick carbonate section with a gas column of up to 300 m. The discovery well was followed by two vertical wells, EX-2 and EX-3, drilled into platform-interior successions that are cored almost continuously. The platform margin and flank, and lateral relationships with siliciclastic strata, are not established by well control and can be inferred only from seismic data.

Previous area studies

The cored reference well EX-2 penetrates the interior platform vertically in a lagoonal position. On a large scale, four different reservoir zones can be delineated from their seismic character, being predominantly either high or low impedance (following Rankey et al. 2019, Figure 2). The five horizons in Figure 2 define five delimiting platform stages. We label the zones A – D, from base to top, each corresponding with its underlying surfaces A – D. Zone A has mostly low impedance strata (particularly in its upper part), and transitions upwards from dominant coral rudstone and floatstone in its lower section into more abundant wackestone to packstone with ample benthic foraminifera and coralline red algae near the top. Strata are dolomitized in zone A. The higher-impedance zone B includes foraminiferal-red algal wackestone to packstone, and an argillaceous interval. The succession of the lower part of zone C has predominantly low impedance, and includes wackestone to packstone with benthic foraminifera and red algae. Locally, it is dolomitized. These deposits pass upwards into less commonly dolomitized floatstone, rudstone, and framestone with corals dominant towards the top of the zone. Finally, zone D is characterized by high impedance layers but shows considerable variability in velocity and density logs, particularly in its upper section. It contains wackestone to packstone, and some grainstone. Internal Petronas reports document the occurrence of planktonic foraminifera in that uppermost interval of the EX-2 core, suggesting a general transgressive trend (Rankey et al. 2019).

The seismic stratigraphy of this platform has been interpreted from 3-D seismic reflection data (Figure 2). Rankey et al. (2019) describe a total of six distinct phases of platform growth. The platform started with a laterally extensive character (stage 0), topped by a succession of back-stepping isolated platforms (stages 1 and 2). Platform stages 3 and 4 are interpreted as temporally distinct *in-situ* reef systems growing along the flanks of the isolated platform of stage 2, potentially during a time when the latter was subaerially exposed. The last phase of carbonate growth (stage 5) is represented by a winged, pinnacle-shaped feature representing the top of the platform.

AVAILABLE DATA AND ANALYSIS

The platform is covered with 3-D seismic data acquired and processed in 2000. The data have been migrated in time and stacked into near- and far-angle cubes. The processed record length is 4 s in total with a sampling interval of 2 ms. The two cubes both contain 594 in-lines, spaced 25 m, and 2577 crosslines, spaced 12.5 m. For this study, the amplitude data along the NW-SE oriented inline that crosses one of the vertical cored wells (EX-2) has been extracted from both near and far stack seismic cubes as input for 2-D seismic inversion (Figure 3). A wavelet extracted for each of the two angle stacks with commercial software reveal a dominant frequency of 20 Hz and 12 Hz for near and far stacks, respectively. The well has a vertical seismic profile with check shots that was used to tie the well to the seismic data. In addition to core, a suite of well logs is available, including P-wave sonic and density (Figure 4). The lack of measured S-wave sonic data for the well is a limitation to the data set and to the study. Therefore, an S-wave sonic run from an EX production well was compared with its P-wave sonic, and results were consistent with Greenberg-Castagna's V_P - V_S relation in carbonate rocks. Assuming similar V_P / V_S ratio trends in the platform, we calculate V_S from V_P, considering a limestone - dolomite distribution curve, based on plug calcimetry data (Greenberg and Castagna 1992). The use of Greenberg-Castagna's relation for S-wave prediction at the calibration well might lead to an overestimation of the correlation between P- and S-wave velocities. Originally, a plug was taken at every foot of core. Those measurements were accessed from a legacy data set. The original plugs, however, were no longer available. A porosity curve calculated from the density log using a linear average (Mavko et al., 2020) based on the mineral parameters in Table 1 was calibrated with measured porosity data from core plugs. The core facies classification was extended to the entire interval of interest by applying to the elastic well logs discriminant analysis using Mahalanobis distance with stratified covariance estimates, a supervised classification method (Grana et al., 2012). The training data set includes the elastic well logs features and the facies labels of core samples.

For this study, carbonate facies are defined based on core description and thin section studies and further analyzed with respect to their elastic properties. For these elastic carbonate facies, lithology is a primary parameter, leading to a subdivision into classes of dolomite, dolomitized limestone, limestone, and shale. A further differentiation is made by pore type, a parameter that has a pronounced effect on elastic properties in carbonates (Eberli et al., 2003; Verwer et al., 2008, Xu and Payne 2009, Zhao et al., 2013, Fournier et al., 2018). The classification includes sucrosic, vuggy, and crystalline dolomite, as well as vuggy and non-vuggy variations of dolomitized limestone, and limestone, respectively. Additionally, argillaceous limestone and shale occur, leading to a total of nine facies (Figure 5).

The relation between porosity, mineralogy and elastic properties in each facies can be investigated using rock physics models (Mavko et al., 2020). The inversion method relies on the statistical parameters, including mean, variance and correlation, of elastic and petrophysical properties in each facies. These parameters can be estimated directly from well log data (data-driven approach) or by using a rock physics model (model-driven approach). Because the inversion method is based on a linearization of the rock physics relations, we make a preliminary validation of the rock physics model at the well location to verify the consistency of the data and their trends with the linearization of the rock physics relations. The proposed rock physics analysis is based on a linearization of Berryman's rock physics model (Berryman, 1997) as shown in de Figueiredo et al. (2017). The rock physics model predicts the elastic properties, velocities and density, as a function of porosity. The bulk and shear moduli and density of the mineral phase are facies dependent and the values are obtained by fitting a linearized rock physics model to the well log data. The optimized parameters are shown in Table 1 and are consistent with measured values available in the literature (Mavko et al., 2020). The variations in the elastic moduli justify the range of the Vp/Vs ratio in the well log data. The density parameters correlate with the dolomite fraction, except for the vuggy limestones and dolomitized limestone where the optimized values are higher than expected, probably due to the limited number of core plug samples or the presence of small fractions of stiffer minerals. The model predictions show that dolomitization increases the shear modulus. All dolomites are characterized by a shear modulus of around 30 GPa, whereas limestones lie around 20 GPa (Table 1). The highest bulk moduli occur in vuggy limestones and dolomitized limestone, showing that a vuggy pore fabric increases the stability of the matrix and the stiffness of the bulk rock (Baechle et al., 2008b). Calcimetry results were used to distinguish among facies. Data show an average dolomite content of about 10% for limestones, 25 - 35% for dolomitized limestone, and greater than 75% for dolomites (Table 1). Displaying log data in velocity – density and velocity – porosity cross plots show that, as a general trend, dolomitic rocks show higher P-wave velocities than limestone at comparable densities and porosities (Figure 6). The rock physics analysis justifies the Bayesian linearized approach in the poro-elastic domain proposed in the Methodology section.

METHODOLOGY

The inversion method is a two-step process that includes the inversion of partial-stack seismic data for elastic properties and the subsequent classification of facies and their porosity from the inverted model parameters. The solution of the inverse problem is highly non-unique due to the limited bandwidth of the seismic data, the low signal to noise ratio, and the heterogeneity of the rock and fluid properties. Therefore, we adopt a hierarchical Bayesian approach to account for the uncertainty in the data and quantify the precision in the estimation of the most-likely facies model. The Bayesian approach to elastic inversion is based on the linearized AVO inversion presented by Buland and Omre (2003). The facies classification and porosity prediction are based on Bayesian petrophysical inversion assuming Gaussian mixture models presented in Grana (2016).

Bayesian seismic inversion is an efficient method for the prediction of the posterior distribution of elastic properties from pre-stack seismic data (Buland and Omre, 2003). The inversion algorithm is based on the convolutional model. From a mathematical point of view, it can be represented as a convolution of a known wavelet with angle-dependent reflection coefficient from the linearized approximation of Zoeppritz equations (Aki and Richards, 2002). This formulation is linear with respect to the logarithm of the elastic properties and it provides a good approximation of the convolutional model with full Zoeppritz equations (Zoeppritz, 1919) for acquisition angles lower than 40°-45° (the maximum reflection angle in the proposed application is 30°). The linearization of the model can be expressed in an analytical form using a product of a matrix $\boldsymbol{G}$ and the model vector $\boldsymbol{m}$

$$\boldsymbol{d} = \boldsymbol{G}\boldsymbol{m} + \boldsymbol{e}, \tag{1}$$

where $\boldsymbol{d}$ represents the data vector, $\boldsymbol{G}$ is the forward geophysical model, $\boldsymbol{m}$ is the vector of the unknown model variables, and $\boldsymbol{e}$ represents the measurement error. In our application, the data include the partial-stack seismograms for two angle stacks (near and far); the forward geophysical model is the convolutional model, and the model vector includes the logarithm of P-wave velocity, S-wave velocity, and density, as in Buland and Omre (2003). Our goal is to predict the probability of the model properties given the seismic data $P(\boldsymbol{m}|\boldsymbol{d})$ using Bayes' rule

$$P(\boldsymbol{m}|\boldsymbol{d}) = P(\boldsymbol{d}|\boldsymbol{m})P(\boldsymbol{m})/P(\boldsymbol{d}). \quad (2)$$

If we assume that the prior distribution $P(\boldsymbol{m})$ of the logarithm of P-wave velocity, S-wave velocity, and density, is a multivariate Gaussian distribution $N(\boldsymbol{m};\boldsymbol{\mu_m},\boldsymbol{\Sigma_m})$ with prior mean $\boldsymbol{\mu_m}$ and prior covariance matrix $\boldsymbol{\Sigma_m}$, and if the measurement errors are assumed to be Gaussian distributed $N(\boldsymbol{e};\boldsymbol{0},\boldsymbol{\Sigma_e})$ with 0 mean and known covariance matrix and they are independent of the model, then the posterior distribution of the model $P(\boldsymbol{m}|\boldsymbol{d})$ is a Gaussian distribution $N(\boldsymbol{m};\boldsymbol{\mu_{m|d}},\boldsymbol{\Sigma_{m|d}})$ and the conditional mean and conditional covariance matrix can be analytically computed (Buland and Omre, 2003):

$$\boldsymbol{\mu_{m|d}} = \boldsymbol{\mu_m} + \boldsymbol{\Sigma_m}\mathbf{G}^T\left(\mathbf{G}\boldsymbol{\Sigma_m}\mathbf{G}^T + \boldsymbol{\Sigma_d}\right)^{-1}(\boldsymbol{d} - \mathbf{G}\boldsymbol{\mu_m}); \quad (3)$$

$$\boldsymbol{\Sigma_{m|d}} = \boldsymbol{\Sigma_m} - \boldsymbol{\Sigma_m}\mathbf{G}^T\left(\mathbf{G}\boldsymbol{\Sigma_m}\mathbf{G}^T + \boldsymbol{\Sigma_d}\right)^{-1}\mathbf{G}\boldsymbol{\Sigma_m}. \quad (4)$$

To account for the lack of low frequencies in the seismic data, we first compute a low-frequency model for the elastic properties obtained by interpolating filtered well log data (filtered at a frequency corresponding to 5 Hz) using ordinary kriging (Doyen, 2007). The logarithm of the so-obtained model is used as a locally varying prior mean $\boldsymbol{\mu_m}$. The prior covariance matrix is estimated from the well logs from the difference between the full resolution well logs and the filtered logs.

The wavelet is estimated from the seismic data for each angle stack. The inversion is performed locally in 1-D, and applied trace by trace by computing at each trace the vector of the posterior mean $\boldsymbol{\mu}_{\boldsymbol{m}|\boldsymbol{d}}$ (i.e., the most likely model) and the diagonal elements of the pointwise covariance matrices $\boldsymbol{\Sigma}_{\boldsymbol{m}|\boldsymbol{d}}$ (i.e., the variances of the model). The posterior distribution of density generally shows greater uncertainty than the elastic properties as shown in Buland and Omre (2003), especially when the far angle is relatively small, as in the proposed application.

Based on the previously obtained elastic properties, we predict the spatial distribution of the facies and their porosity. The statistical model for the facies classification and porosity inversion is a Gaussian mixture model where the weights of the mixture are the probability of the facies and the Gaussian components represent the distribution of porosity conditioned on elastic properties within each facies (Grana, 2016). We adopt a hierarchical Bayesian approach to predict the posterior probability $P(f,\phi|\boldsymbol{m})$ of facies and porosity given the most likely model of elastic properties (in the following $\boldsymbol{\mu}_{\boldsymbol{m}|\boldsymbol{d}}$ is replaced by $\boldsymbol{m}$ to simplify the notation).

We assume that the distribution of porosity is Gaussian within each facies. Because Gaussian distributions are defined in the entire set of real numbers we introduce truncations to avoid porosity values that fall outside the physical ranges. The prior distribution of porosity is then a Gaussian mixture

$$P(\phi) = \sum_{f=1}^{F} P(f) N(\phi; \mu_\phi^{(f)}, \sigma_\phi^{(f)}), \tag{5}$$

where F is the number of facies, $\mu_\phi^{(f)}$ represents the prior mean of porosity in each facies, and $\sigma_\phi^{(f)}$ is the prior standard deviation. In this formulation, the weights of the Gaussian mixture are the facies proportions $P(f)$.

We assume a multi-linear relationship on each facies between porosity and the elastic properties and we estimate the marginal posterior distributions $P(f|\boldsymbol{m})$ and $P(\phi|\boldsymbol{m})$ by analytically computing the parameters of the posterior Gaussian mixture model

$$P(\phi|\boldsymbol{m}) = \sum_{f=1}^{F} P(f|\boldsymbol{m}) N(\phi; \mu_{\phi|\boldsymbol{m}}^{(f)}, \sigma_{\phi|\boldsymbol{m}}^{(f)}), \tag{6}$$

as in Grana (2016). At each point where data are available, the set of posterior parameters includes the posterior probability $P(f \mid \boldsymbol{m})$ of the facies conditioned by the elastic properties, the conditional means of porosity $\mu_{\phi|\boldsymbol{m}}^{(f)}$, and the conditional standard deviations $\sigma_{\phi|\boldsymbol{m}}^{(f)}$ in each facies. They can be calculated as

$$P(f|\boldsymbol{m}) = \frac{N(\boldsymbol{m}; \boldsymbol{\mu}_{\boldsymbol{m}}^{(f)}, \boldsymbol{\Sigma}_{\boldsymbol{m}}^{(f)}) P(f)}{\sum_{k=1}^{F} P(k) N(\boldsymbol{m}; \boldsymbol{\mu}_{\boldsymbol{m}}^{(k)}, \boldsymbol{\Sigma}_{\boldsymbol{m}}^{(k)})} \qquad f = 1,\ldots,F \tag{7}$$

$$\mu_{\phi|\boldsymbol{m}}^{(f)} = \mu_{\phi}^{(f)} + \boldsymbol{\Sigma}_{\phi,\boldsymbol{m}}^{(f)} \left(\boldsymbol{\Sigma}_{\boldsymbol{m}}^{(f)}\right)^{-1} (\boldsymbol{m} - \boldsymbol{\mu}_{\boldsymbol{m}}^{(f)}); \tag{8}$$

$$\sigma_{\phi|\boldsymbol{m}}^{(f)} = \sqrt{\left(\sigma_{\phi}^{(f)}\right)^{2} - \boldsymbol{\Sigma}_{\phi,\boldsymbol{m}}^{(f)} \left(\boldsymbol{\Sigma}_{\boldsymbol{m}}^{(f)}\right)^{-1} \left(\boldsymbol{\Sigma}_{\boldsymbol{m},\phi}^{(f)}\right)^{T}}. \tag{9}$$

where $\boldsymbol{\mu}_{\boldsymbol{m}}^{(f)}$ *and* $\boldsymbol{\Sigma}_{\boldsymbol{m}}^{(f)}$ are the mean and covariance matrices of the elastic properties conditioned by facies, and $\boldsymbol{\Sigma}_{\phi,\boldsymbol{m}}$ is the cross - covariance matrix of porosity and the elastic parameters. The Gaussian mixture model that describes the likelihood of elastic properties conditioned by facies is shown in Figure 7. In general, facies show higher likelihoods when the variances are comparatively low, resulting in a better prediction of sharper peaks in the Gaussian curves. In total, at each point, we estimate $3F-1$ parameters: F conditional means, F conditional standard deviations, and $F-1$ conditional probabilities of facies (since the sum must be 1).

To correctly propagate the uncertainty for the seismic data to the petrophysical properties, we should apply the Chapman-Kolmorogov theorem (Grana and Della Rossa, 2010) and compute the integral of the conditional Log-Gaussian distribution with parameters in equations 3-4 and the conditional Gaussian mixture distribution with parameters in equations 7-9; however, the integral cannot be analytically solved and requires numerical evaluation. To reduce the computational cost, we compute the posterior distribution using a hierarchical approach, where we sequentially compute the probability distributions in equations 3-4 and in equations 7-9. This approach generally provides accurate results but might lead to an underestimation of the model uncertainty (Grana and Della Rossa, 2010).

RESULTS

We first apply the inversion method for elastic properties to the seismic data and extract the inverted trace at the well location. The inverted data are characterized by markedly lower resolution than the original logs, but the inversion successfully captures the reservoir zonation, marking higher impedance in Zones B and D, for example (Figure 8). The top-carbonate pick at the EX-2 well position appears at around 1.5s as a downward increase in velocities and densities, corresponding with horizon E of Rankey et al. (2019) (Figures 2 and 4). Below that interval, two sets of high- and low-velocity zones are captured by the inverted trace. In the 2-D inversion results (Figure 9), the shape of the carbonate platform to the NW of the well (crosslines 2250 to 2420) is evident as a zone of velocities and densities elevated relative to the overlying strata (Figure 10). Within the platform, both high and low velocity packages show considerable variability, reflecting complex multi – stage growth of the carbonate platform (Rankey et al., 2019). The apparent breaks and vertical jumps of high velocity packages towards the south eastern flank of the platform can be interpreted as faults.

We then apply the facies prediction algorithm to upscaled well log data, the extracted seismic trace at the well location, and the inline cross-cutting the platform from NW to SE. For the well log data, the facies log is first resampled at 2 ms to equal the seismic sampling rate (Figure 11a, 11b). For discrete facies data, the most probable facies in each 2 ms interval is chosen. On comparing the inversion results from resampled log data with the actual facies from core, limestone, vuggy limestone, and vuggy dolomitized limestone facies are consistently predicted. (Figure 11c). Layers of sucrosic dolomite (pink), a facies of particular interest due to its favorable reservoir properties, are likely to be classified as vuggy dolomitized limestone (dark green), due to a considerable overlap of its elastic parameters (Figure 7). In the interval of interest (Zone A – D), dolomites (purple shades) only appear on three counts in the maximum-a-posteriori (MAP) prediction, one sucrosic dolomite layer in Zone C, one vuggy and one crystalline dolomite layer in Zone D (Figure 11c). Yet, probability analysis demonstrates that dolomitic facies are not "lost" by the inversion algorithm, and reveals increased dolomite probabilities at their actual positions of occurrence in the core column, especially at 1.50-1.52 s (Zone D), 1.57-1.58 s (Zone C), and at around 1.65-1.67 s (lower Zone A, Figure 11 D). The inverted porosity log from the upscaled elastic well log data matches the trends in the measured porosity (Figure 11e). The porosity inversion also captures the tight section in zone B, which includes an argillaceous limestone layer.

The subsequent application replaces the input data with the seismic trace extracted at the well location, tied to the logs with check shots. For comparison, original and upscaled lithology are shown again in Figure 12a and 12b, but the prediction of lithologies and facies occur at much lower resolutions, using the seismic trace as input (Figure 12c-12e). The MAP solution of facies inverted from seismic data at the well location predicts high porosity sections as vuggy dolomitized limestones, low porosity zones as limestone, and transitional zones as vuggy limestone. The dolomite probabilities remain low (below 0.2) in the inferred solution from seismic data at the well location. The low resolution determines a difficulty to detect elastically distinct features below an estimated thickness of around 50 m. (Figure 12c and 12d). An alternative approach to improve the classification would require the clustering of different facies into a smaller number of broadly defined seismic facies (Grana et al., 2017).

The result of the 2D inversion shows the platform pinnacle between crosslines 2300 and 2400 as an asymmetrically domed feature (Figure 13a). The lower (below 1.5 s TWT) part of the feature appears to be layered horizontally, and probability analysis for vuggy dolomitized limestone, a preferred reservoir facies, reveals the likely occurrence of an elongated high flow zone about 2 km across and 0.05 s thick (Figure 13b). This is in agreement with the porosity result, showing increasing values toward the SE side (Figure 13c).

DISCUSSION

Our algorithm is based on a Bayesian approach for discrete and continuous properties and is implemented in terms of elastic properties and density. Other parameterizations, for example in terms of impedance and V_P / V_S ratio could be adopted. The proposed approach does not include spatial correlations of the facies. Advanced formulations including a spatial correlation model, such as hidden Markov models (Lindberg and Grana, 2015), could be introduced, but the parameter estimation is challenging due to the large number of facies.

The distributions of elastic carbonate facies for vuggy and crystalline dolomites display standard deviations larger than those of limestone and dolomitized limestone facies, especially for velocity data in this study. The P- and S-wave velocity means for sucrosic dolomite nearly equal those of vuggy dolomitized limestone (Figure 7). The inversion results underpredict the occurrence of dolomite, incorporating it into more dominant facies. This becomes evident especially in the inversion result of the seismic trace given its low resolution. The sucrosic dolomites in zones A and C are classified as vuggy dolomitized limestone, predominantly. Vuggy and crystalline dolomite are predicted as part of a limestone or vuggy limestone section in zone A, but also vuggy dolomitized limestone in zone C (Figure 12c). The overlap of S-wave velocity and density distributions for vuggy limestone and vuggy dolomitized limestone facies is considerable, increasing the uncertainty in the predictions (Figure 7).

To provide context to the inversion results, we apply the interpretation framework of Epting (1980) and seismic-stratigraphic interpretation of Rankey et al (2019) to the 2-D inversion result (Figure 14). The first platform stage, represented by zone A in core and capped by horizon B (red), is predicted to show an upward transition from vuggy limestone to limestone, and to vuggy limestone again. Lower zone A, which is richer in dolomite in core, is inferred as vuggy limestone, equally as upper zone A, where the prediction is correct. Interbedded dolomite – limestone strata tend to be inferred as vuggy limestone, or vuggy dolomitized limestone for higher porosities, as in middle zone A, when averaged to the resolution of the seismic data. Within that large-scale observational framework, adapted to seismic resolution, vuggy limestone also appears to be a transitional facies between limestone, which is predicted for high-impedance layers, and vuggy dolomitized limestone, the predicted facies in low impedance sequences.

The second platform stage, an isolated one including zones B and C, marks a pronounced back step with regard to the first platform. Zone B is dominated by limestone in basal strata, which contains an argillaceous layer (in core) that likely represents the initial flooding. The 2-D inversion predicts a lateral transition from limestone to vuggy limestone and vuggy dolomitized limestone within this interval in the central part of the platform (Figure 14). Above this, in zone C, this second platform stage transitions into vuggy dolomitized limestone, forming an isolated platform (6-8 km across), which contains some of the highest porosity in the entire system (Figure 13c). The build-up developing during this growth stage has been interpreted as shallow-water isolated platform, deposited at a time of structural activity. Across a normal fault, stratal thickening on the downthrown block contrasts with thinner strata on the upthrown block, near the eastern platform margin (Rankey et al. 2019). The facies inversion result reveals consistent time thickness changes across the fault, most evident within basal limestone strata and displacement of horizon B. The 2-D inversion predicts that the high porosity, vuggy dolomitized limestone and sucrosic dolomite facies continues on the upthrown fault block to the southeast (Figure 14). However, previous interpretations (Epting, 1980; Bracco-Gartner et al., 2004; Rankey et al., 2019) have suggested that the basinal strata surrounding and overlying the platform are siliciclastics. This misinterpretation occurs because the algorithm applied in this study is not trained to distinguish between siliciclastic and carbonate strata but focuses on defining subtle differences in carbonate facies. A sandstone or mudstone in these off-platform areas would be classified by its elastic properties into one of the predefined carbonate facies.

The subsequent third stage of platform growth comprising zone D consists of a basal limestone package with planktonic foraminifera that has been interpreted to represent a relative rise in sea level, and flooding of the previous platform (Rankey et al. 2019). This interval is overlain and downlapped by, a smaller, backstepped, shallow-water isolated platform roughly 1 km across in this seismic section. The training well EX-2 penetrates only thin downdip strata of the platform at this stage. The platform is capped by horizon E, and in the inversion, its thickest part is predicted to consist of vuggy dolomitized limestone and shale. In seismic data, this platform represents a ~1 km x 5 km North-South oriented layer, whose top continues to the EX-2 well location, where the corresponding strata in core does not include shale, and it is therefore unlikely that the thickest part of the platform does. Nonetheless, an uncored well penetrating this zone shows elevated gamma ray in wireline logs, potentially suggesting shale occurrence. Yet, dolomite can be associated with elevated uranium levels, affecting gamma ray measurements. Shell legacy descriptions characterize the interval as mouldic sucrosic dolomite, making the inversion prediction of shale likely incorrect. The training data from the EX-2 core included sucrosic dolomite, and vuggy dolomite, yet no mouldic sucrosic dolomite. The latter might well be an occurring lithofacies, which has not been sampled in core and has been classified, due to its elastic behavior, incorrectly as shale.

Stages four and five of Rankey et al. (2019), here described as one phase, appear as wedges of limestone that onlap the margins of the older isolated platform. The easterly wedge has been interpreted as reef systems developed along the margins of the previous isolated platform (e.g., capped by Horizon E) during its subaerial exposure. The last phase of platform growth, capped by horizon T, shows a transition from limestone to shale to vuggy dolomitized limestone from NW towards SE (Figure 14). The character of the platform architecture also includes wedge-shaped carbonate bodies on the western platform flank. The top carbonate, Horizon T, can be identified in the log signature of the cored well as carbonate stringer, which is not resolved by the facies inversion based on seismic data (Figure 14).

CONCLUSIONS

We applied a Bayesian inversion for nine facies in a carbonate platform, outlining the strengths and weaknesses of the method, which extends from core to wellbore to seismic data. The results have been integrated with an independent seismic stratigraphic and geological interpretation, derived from reflection seismic data, providing a probabilistic model of the platform architecture that includes predictions of elastic parameters, porosity, and facies. The results integrated with a literature review demonstrate that the isolated carbonate platform nucleated from an initial extensional structural high, followed by two phases of back-stepping. Subsequent wedge-shaped carbonate systems onlap the margins of the older isolated platform. A last phase of growth led to a pinnacle at the top, before the entire platform eventually drowned and was buried by siliciclastic sediment. For platform stages one and two, our study predicts an upwards transition towards high porosity vuggy dolomitized limestone facies, possibly coinciding with depositional shallowing upward during each platform stage. The facies inversion is consistent with stratal thinning across a normal fault at the eastern platform margin, a result of structural activity at the time of deposition. The third stage, a small isolated platform, is also characterized by a transition from limestone towards higher porosity facies, most probably a mouldic sucrosic dolomite, which has not been sampled in the reference core and hence is mispredicted as shale. The results of carbonate facies prediction by Bayesian inversion appear promising for well data applications, but require geological prior support. The extension to seismic and spatial prediction yields valuable results, too, if compared to and embedded within a solid geologic - stratigraphic interpretation as contextual framework.

DOI:10.1190/geo2020-0361.1

REFERENCES

Aki, K. and P. G. Richards, 2002, Quantitative seismology: University Science Books

Avseth P., T. Mukerji, and G. Mavko, 2005, Quantitative Seismic Interpretation. Applying Rock Physics Tools to Reduce Interpretation Risk: Cambridge University Press.

Baechle G. T, A. Colpaert, G. P. Eberli, and R. J. Weger, 2008a, Effects of microporosity on sonic velocity in carbonate rocks: The Leading Edge **27**, 1012-1018.

Baechle G. T., G. P. Eberli, A. Boyd, J. M. DeGrange, and L. Al-Kharusi, 2008b, Oomoldic carbonates: Pore structure and fluid effects on sonic velocity: SEG Annual Meeting 2008, Extended Abstracts, 1660-1664.

Baechle G. T., G. P. Eberli, R. J. Weger, and J. L. Massaferro, 2009, Changes in dynamic shear moduli of carbonate rocks with fluid substitution: Geophysics **74**, no. 3, E135-E147.

Berryman, J.G., 1997, Generalization of Eshelby's formula for a single ellipsoidal elastic inclusion to poroelasticity and thermoelasticity: Physical Review Letters, **79**, 1142-1145.

Bracco-Gartner, G. L., W. Schlager, and E. W. Adams, 2004, Seismic expression of the boundaries of a Miocene carbonate platform, Sarawak, Malaysia, *in* G. P. Eberli, J. L. Masaferro, J. F. "Rick" Sarg, eds., Seismic imaging of carbonate reservoirs and systems: AAPG Memoir **81**, 351– 365.

Buland A. and H. Omre, 2003, Bayesian linearized AVO inversion: Geophysics **68**. 185-198.

de Figueiredo L. P., D. Grana, M. Santos, W. Figueiredo, M. Roisenberg, and G. S. Neto, 2017, Bayesian seismic inversion based on rock-physics prior modeling for the joint estimation of acoustic impedance, porosity and lithofacies: Journal of Computational Physics **336**, 128–142.

Dou Q., Y. F. Sun and C. Sullivan, 2011, Rock-physics-based carbonate pore type characterization and reservoir permeability heterogeneity evaluation, upper San Andres reservoir, Permian Basin, West Texas: Journal of Applied Geophysics **74**, 8–18.

Doyen, P., 2007, Seismic reservoir characterization: EAGE Publications.

Eberli G. P., G. T. Baechle, F. S. Anselmetti, and M. L. Incze, 2003, Factors controlling elastic properties in carbonate sediments and rocks: The Leading Edge **22**, 654-660.

Epting, M., 1980, Sedimentology of Miocene Carbonate Buildups, Central Luconia, Offshore Sarawak: Bulletin of the Geological Society of Malaysia, **12**, 17-30.

Fournier, F., M. Pellerin, Q. Villeneuve, T. Teillet, F. Hong, E. Poli, J. Borgomano, L. Philippe, and A. Hairabian, 2018, The equivalent pore aspect ratio as a tool for pore type prediction in carbonate reservoirs: AAPG Bulletin, **7**, 1343–1377

Fui, H. K., 1978, Stratigraphic framework for oil exploration in Sarawak: Bulletin of the Geological Society of Malaysia, **10**, 1-13.

Ghon, G., E.C. Rankey, G.T. Baechle, M. Schlaich, S.H. Ali, S. Mokhtar and M.C. Poppelreiter, 2018, Carbonate Reservoir Characterisation of an Isolated Platform Integrating Sequence Stratigraphy and Rock Physics in Central Luconia, Sarawak Basin, Malaysia: 80th EAGE Conference and Exhibition, Extended Abstracts.

Grana, D. and E. Della Rossa, 2010, Probabilistic petrophysical properties estimation integrating statistical rock physics with seismic inversion: Geophysics **75**, no. 3, O21–O37.

Grana, D., M. Pirrone, M. and T. Mukerji, 2012, Quantitative log interpretation and uncertainty propagation of petrophysical properties and facies classification from rock-physics modeling and formation evaluation analysis: Geophysics, **77**, no. 3, WA45-WA63.

Grana, D., 2016, Bayesian linearized rock-physics inversion: Geophysics **81**, no. 6, D625-D641.

Grana, D., X. Lang, and W. Wu, 2017, Statistical facies classification from multiple seismic attributes: comparison between Bayesian classification and expectation–maximization method and application in petrophysical inversion: Geophysical Prospecting, **65**, 544-562.

Grana, D., 2018, Joint facies and reservoir properties inversion: Geophysics **83**, no. 3, M15-M24.

Grana, D., L. Azevedo, and M. Liu, 2020, A comparison of deep machine learning and Monte Carlo methods for facies classification from seismic data: Geophysics, **85**, no. 4, WA41-WA52.

Greenberg, M.L. and J.P Castagna, 1992, Shear-wave velocity estimation in porous rocks: theoretical formulation, preliminary verification and applications. Geophysical Prospecting **40**, 195–209.

Hall, R., 2012, Late Jurassic–Cenozoic reconstructions of the Indonesian region and the Indian Ocean: Tectonophysics **570-571**, 1–41.

Hall, R. and W. Spakman, 2015, Mantle structure and tectonic history of SE Asia: Tectonophysics **658**, 14–45.

Hageman, H., 1987, Palaeobathymetrical changes in NW Sarawak during Oligocene to Pliocene times: Bulletin of the Geological Society of Malaysia **21**, 91-102.

Karimpouli S., H. Hassani, M. Nabi-Bidhendi, H. Khoshdel and A. Malehmir, 2013, Application of probabilistic facies prediction and estimation of rock physics parameters in a carbonate reservoir from Iran: Journal of Geophysical Engineering **10**, 1-14.

Koša E., G. M. D. Warrlich, and G. Loftus, 2015, Wings, mushrooms, and Christmas trees: The carbonate seismic geomorphology of Central Luconia, Miocene–present, offshore Sarawak, northwest Borneo: AAPG Bulletin **99**, 2043–2075.

Lindberg, D. and D. Grana, 2015, Petro-elastic log-facies classification using the expectation–maximization algorithm and hidden Markov models. Mathematical Geosciences **47**, 719-752.

Liu, J., X. Dai, L. Gan, L. Liu, and W. Lu, 2018, Supervised seismic facies analysis based on image segmentation: Geophysics, **83**, no. 2, O25-O30.

Liu, M., M. Jervis, W. Li, and P. Nivlet, 2020, Seismic facies classification using supervised convolutional neural networks and semisupervised generative adversarial networks: Geophysics, **85**, no. 4, O47-O58.

Lunt P. and M. Madon, 2017, A review of the Sarawak Cycles: history and modern application: Bulletin of the Geological Society of Malaysia **63**, 77-101.

Mavko, G., T. Mukerji, and J. Dvorkin, 2020, The rock physics handbook: Cambridge University Press.

Rankey E. C., M. Schlaich, S. Mokhtar, G. Ghon, S. H. Ali, and M. Poppelreiter, 2019, Seismic architecture of a Miocene isolated carbonate platform and associated off-platform strata (Central Luconia Province, offshore Malaysia): Marine and Petroleum Geology **102**, 477–495.

Steuer S., D. Franke, F. Meresse, D. Savva, M. Pubellier, and J. L. Auxietre, 2014, Oligocene - Miocene carbonates and their role for constraining the rifting and collision history of the Dangerous Grounds, South China Sea: Marine and Petroleum Geology **58**, 644-657.

Sun, Y. F., 2000, Core-log-seismic integration in hemipelagic marine sediments on the eastern flank of the Juan De Fuca Ridge. In: Proceedings of Ocean Drilling Program Science Results **168**, 21-35.

Sun Y. F., 2004, Effects of pore structure on elastic wave propagation in rocks, AVO modelling: Journal of Geophysics and Engineering **1**, 268–276.

Verwer, K., H. Braaksma, and J. A. M. Kenter, 2008, Acoustic properties of carbonates: Effects of rock texture and implications for fluid substitution: Geophysics **73**, no. 2, B51-B65.

Warrlich, G. M. D., C. Taberner, W. Asyee, B. Stephenson, M. Esteban, M. Boya-Ferrero, A. Dombrowski, and J. H. van Konijnenburg, 2010, The impact of post-depositional processes on reservoir properties: Two case studies of tertiary carbonate buildup gas fields in Southeast Asia (Malampaya and E11), *in* Cenozoic carbonate systems of Australasia: Society for Sedimentary Geology Special Publication **95**, 99-127.

Xu, S., and M. A. Payne, 2009, Modeling elastic properties in carbonates rocks: The Leading Edge, 28(1), 66–74.

Zampetti V., W. Schlager, J. H. v. Konijnenburg, and A. J. Everts, 2004a, Architecture and growth history of a Miocene carbonate platform from 3D seismic reflection data; Luconia province, offshore Sarawak, Malaysia: Marine and Petroleum Geology **21**, 517–534.

Zampetti V., W. Schlager, J. H. v. Konijnenburg, and A. J. Everts, 2004b, 3-D Seismic characterization of submarine landslides on a Miocene carbonate platform (Luconia Province, Malaysia): Journal of Sedimentary Research **74**, 817–830.

Zhang, G. Y., Z. Z. Wang, and Y. K. Chen, 2018, Deep learning for seismic lithology prediction: Geophysical Journal International, **215**, 1368–1387.

Zhao L., J. Geng, J. Cheng, D. Han, and T. Guo, 2014, Probabilistic lithofacies prediction from prestack seismic data in a heterogeneous carbonate reservoir: Geophysics **79**, no. 5, M25-M34.

Zhao, L., M. Nasser, and D. H. Han, 2013, Quantitative geophysical pore-type characterization and its geological implication in carbonate reservoirs: Geophysical Prospecting, 61, 827–841.

Zhou, K., J. Zhang, Y. Ren, Z. Huang, and L. Zhao, 2020, A gradient boosting decision tree algorithm combining synthetic minority over-sampling technique for lithology identification: Geophysics, **85**, no. 4, WA147-WA158.

Zoeppritz, K., 1919, On the reflection and propagation of seismic waves. Gottinger Nachrichten, 1(5), 66-84.

LIST OF FIGURES

Figure 1: (a) Location map of the Sarawak Basin and Central Luconia province on the northern shelf of Borneo, indicated by the red box. (b) Overview of Central Luconia isolated carbonate platforms (red) on structural highs (shaded gray). The study platform in the EX field is marked by the blue box. Additionally, the map shows a network of NE-SW trending faults that document structural activity. Figure modified from Epting (1980), Hall (2012), Koša et al. (2015), Rankey et al. (2019).

Figure 2: Seismic-stratigraphic interpretation of Field EX. (a) Quadrature-phase data, illustrating stratal architecture. (b) Schematic summary of horizons that define five platform stages, and their relation to basinal strata. Modified from Rankey et al. (2019).

Figure 3: Partial angle stacks (a - near and b - far) of seismic reflectivity data extracted from 3-D volumes. These data represent sections that cross the EX platform. The main carbonate build-up is delineated by the yellow rectangle. The well EX-2 trajectory is represented by the blue line.

Figure 4: Wireline Log data from well EX-2: (a)P- and (b) S-wave velocities, (c) density, (d) porosity, and (e) water saturation; (f) core data with facies classification, (g) extrapolated by supervised classification to fill core gaps (see text for details). Facies are classified from core and appear in the legend in the following order: sucrosic dolomite (pink), vuggy dolomite (magenta), vuggy dolomitized limestone (dark green), vuggy limestone (dark blue), crystalline dolomite (purple), dolomitized limestone (light green), limestone (light blue), argillaceous limestone (brown), (calcareous) shale (black). Horizons A – E delineate the reservoir zone boundaries, dividing zones A - D (adapted from Rankey et al. 2019).

Figure 5: Thin section images (scale bar A – H: 1mm; I: 500 μm) of facies, illustrating the range of lithology and pore types. (a) Limestone with mainly intercrystalline and mouldic porosity. (b) Dolomitic limestone with dominantly intercrystalline porosity. (c) Argillaceous limestone with minor fracture porosity. (d) Vuggy limestone. (e) Vuggy dolomitic limestone. (f) Vuggy dolomite. (g) Sucrosic dolomite with intercrystalline porosity. (h) Crystalline dolomite. (i) Calcareous shale.

Figure 6: Relations between log petrophysics (Figure 4) and facies (Figure 5). (a) Cross plot of P-wave velocity versus density, colour coded by facies: sucrosic dolomite (pink), vuggy dolomite (magenta), vuggy dolomitized limestone (dark green), vuggy limestone (dark blue), crystalline dolomite (purple), dolomitized limestone (light green), limestone (light blue), argillaceous limestone (brown), and calcareous shale (black). Dolomites show higher P-wave velocities than limestones at comparable densities. Vuggy limestone and vuggy dolomitized limestone have lower densities than non-vuggy varieties, at the same velocity. (b) Cross plot of P-wave velocity versus porosity, colour coded by facies. For a given porosity, P-wave velocity is generally higher in dolomites. Lines represent facies – dependent Berryman's rock physics models (Berryman, 1997).

Figure 7: Probability density functions (PDFs) describing the Gaussian likelihood of P-wave velocity (a), S-wave velocity (b), and density (c) for each facies, derived from log training data. High porosity sucrosic and vuggy facies show considerably lower mean values and higher overlap of P- and S-wave velocity functions than non-vuggy varieties. Vuggy and crystalline dolomites exhibit higher variance compared to other facies, particularly in (a) and (b).

Figure 8: Elastic properties and density trends. Inverted P-wave velocity (a), S-wave velocity (b), and density (c) from seismic trace extracted at the EX-2 well location (green), compared with the well-log data filtered at 2 ms (black). Reservoir horizons A-T were adapted from

Rankey et al. (2019). Note that the inverted trace captures the log trends well but does not recover peak values due to smoothing. See, for example, the inverted density, between horizons B and C, at around 1.59 s.

Figure 9: 2-D inversion of inline for (a) P-wave velocity, (b) S-wave velocity, and (c) density. The triangle shows the location of the borehole.

Figure 10: Zoom of 2-D inversion of inline for P-wave velocity. Horizons A – E delineate the reservoir zone boundaries, dividing zones A - D (adapted from Rankey et al. 2019).

Figure 11: Inversion results from well data. (a) Actual facies from core in time domain. (b) Actual facies from core, upscaled to seismic sampling rate of 2 ms. (c) Predicted facies resulting from 1-D inversion at well location with upscaled (2 ms) elastic and density well log data as inputs. (d) Probabilities of individual facies. (e) Predicted porosity from 1-D inversion at well location (red) using upscaled (2 ms) elastic and density well log data as inputs.

Figure 12: Inversion results from seismic data at well EX-2 trace. (a) Actual facies from core in time domain. (b) Actual facies from core, upscaled to seismic sampling rate of 2 ms. (c) Predicted facies resulting from 1-D inversion at well location with extracted seismic trace as input. (d) Probabilities of individual facies. (e) Predicted porosity from 1-D inversion at well location (red) using extracted seismic trace as input.

Figure 13: 2-D inversion of extracted inline that crosses EX-2 well location. (a) Facies results displayed as the maximum value. The red box is displayed in Figure 14 with an interpretation framework. (b) probability of vuggy dolomitized limestone, a preferential reservoir facies. An elongated reservoir body is encircled by a black dashed line. (c) Inversion result for porosity. The reservoir body in (b) shows increasing porosity values toward southeast. The well EX-2 is located at trace 2410.

Figure 14: Interpreted 2-D facies inversion of EX carbonate platform, showing reservoir horizons and reference well EX-2 (orange). At the well location, the 1-D facies inversion result from the extracted seismic trace is shown for comparison.

LIST OF TABLES

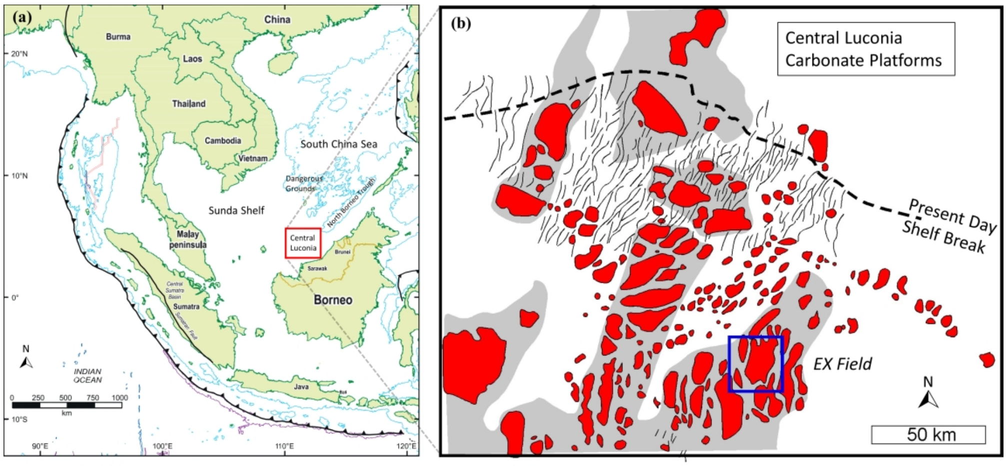

Figure 1: (a) Location map of the Sarawak Basin and Central Luconia province on the northern shelf of Borneo, indicated by the red box. (b) Overview of Central Luconia isolated carbonate platforms (red) on structural highs (shaded gray). The study platform in the EX field is marked by the blue box. Additionally, the map shows a network of NE-SW trending faults that document structural activity. Figure modified from Epting (1980), Hall (2012), Koša et al. (2015), Rankey et al. (2019).

338x190mm (300 x 300 DPI)

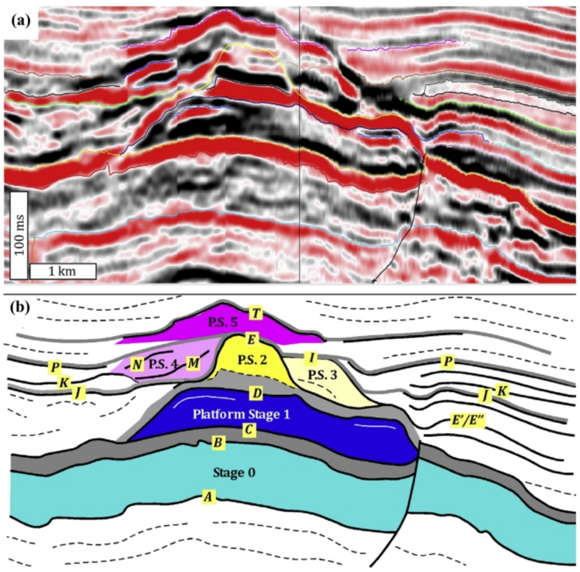

Figure 2: Seismic-stratigraphic interpretation of Field EX. (a) Quadrature-phase data, illustrating stratal architecture. (b) Schematic summary of horizons that define five platform stages, and their relation to basinal strata. Modified from Rankey et al. (2019).

338x190mm (300 x 300 DPI)

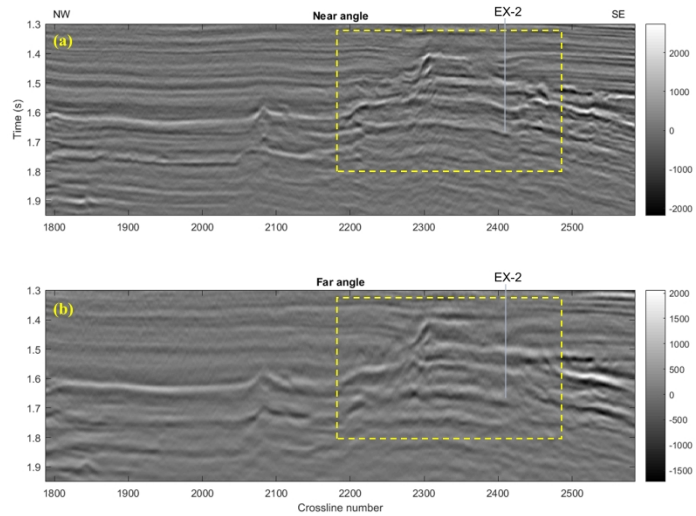

Figure 3: Partial angle stacks (a - near and b - far) of seismic reflectivity data extracted from 3-D volumes. These data represent sections that cross the EX platform. The main carbonate build-up is delineated by the yellow rectangle. The well EX-2 trajectory is represented by the blue line.

338x190mm (300 x 300 DPI)

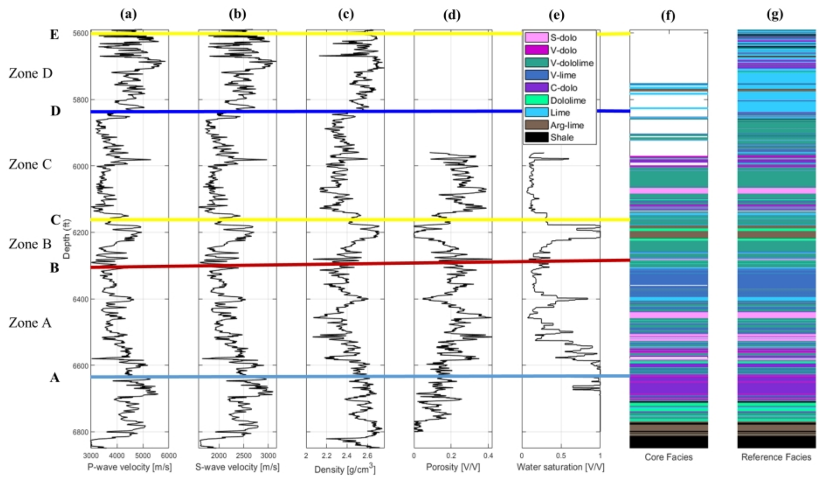

Figure 4: Wireline Log data from well EX-2: (a)P- and (b) S-wave velocities, (c) density, (d) porosity, and (e) water saturation; (f) core data with facies classification, (g) extrapolated by supervised classification to fill core gaps (see text for details). Facies are classified from core and appear in the legend in the following order: sucrosic dolomite (pink), vuggy dolomite (magenta), vuggy dolomitized limestone (dark green), vuggy limestone (dark blue), crystalline dolomite (purple), dolomitized limestone (light green), limestone (light blue), argillaceous limestone (brown), (calcareous) shale (black). Horizons A – E delineate the reservoir zone boundaries, dividing zones A - D (adapted from Rankey et al. 2019).

338x190mm (300 x 300 DPI)

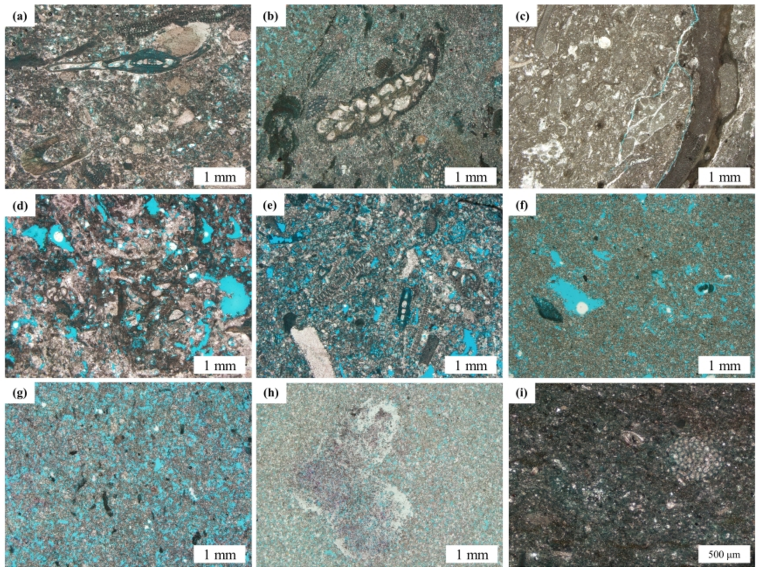

Figure 5: Thin section images (scale bar A – H: 1mm; I: 500 μm) of facies, illustrating the range of lithology and pore types. (a) Limestone with mainly intercrystalline and mouldic porosity. (b) Dolomitic limestone with dominantly intercrystalline porosity. (c) Argillaceous limestone with minor fracture porosity. (d) Vuggy limestone. (e) Vuggy dolomitic limestone. (f) Vuggy dolomite. (g) Sucrosic dolomite with intercrystalline porosity. (h) Crystalline dolomite. (i) Calcareous shale.

338x190mm (300 x 300 DPI)

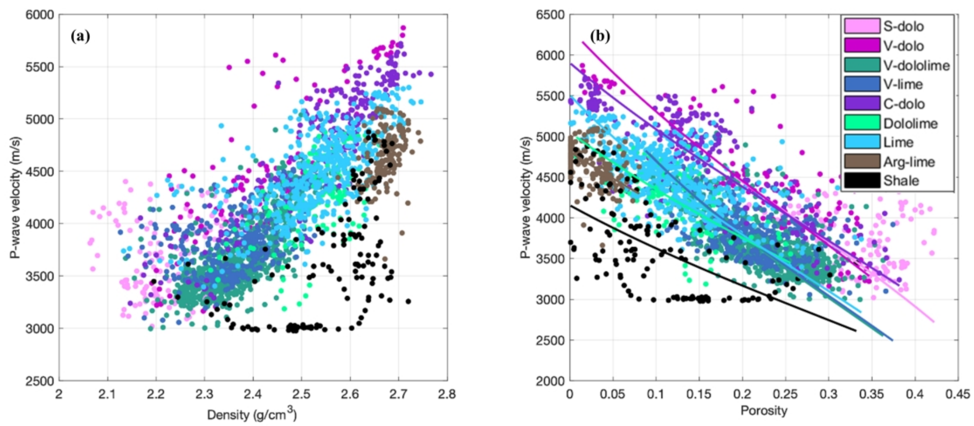

Figure 6: Relations between log petrophysics (Figure 4) and facies (Figure 5). (a) Cross plot of P-wave velocity versus density, colour coded by facies: sucrosic dolomite (pink), vuggy dolomite (magenta), vuggy dolomitized limestone (dark green), vuggy limestone (dark blue), crystalline dolomite (purple), dolomitized limestone (light green), limestone (light blue), argillaceous limestone (brown), and calcareous shale (black). Dolomites show higher P-wave velocities than limestones at comparable densities. Vuggy limestone and vuggy dolomitized limestone have lower densities than non-vuggy varieties, at the same velocity. (b) Cross plot of P-wave velocity versus porosity, colour coded by facies. For a given porosity, P-wave velocity is generally higher in dolomites. Lines represent facies – dependent Berryman's rock physics models (Berryman, 1997).

338x190mm (300 x 300 DPI)

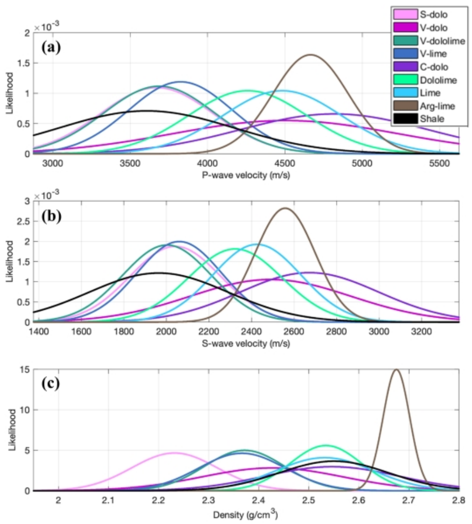

Figure 7: Probability density functions (PDFs) describing the Gaussian likelihood of P-wave velocity (a), S-wave velocity (b), and density (c) for each facies, derived from log training data. High porosity sucrosic and vuggy facies show considerably lower mean values and higher overlap of P- and S-wave velocity functions than non-vuggy varieties. Vuggy and crystalline dolomites exhibit higher variance compared to other facies, particularly in (a) and (b).

338x190mm (300 x 300 DPI)

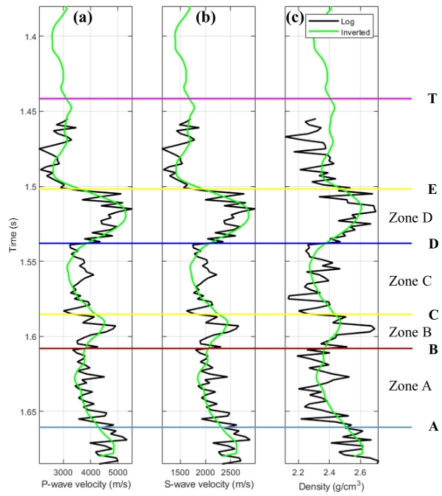

Figure 8: Elastic properties and density trends. Inverted P-wave velocity (a), S-wave velocity (b), and density (c) from seismic trace extracted at the EX-2 well location (green), compared with the well-log data filtered at 2 ms (black). Reservoir horizons A-T were adapted from Rankey et al. (2019). Note that the inverted trace captures the log trends well but does not recover peak values due to smoothing. See, for example, the inverted density, between horizons B and C, at around 1.59 s.

338x190mm (300 x 300 DPI)

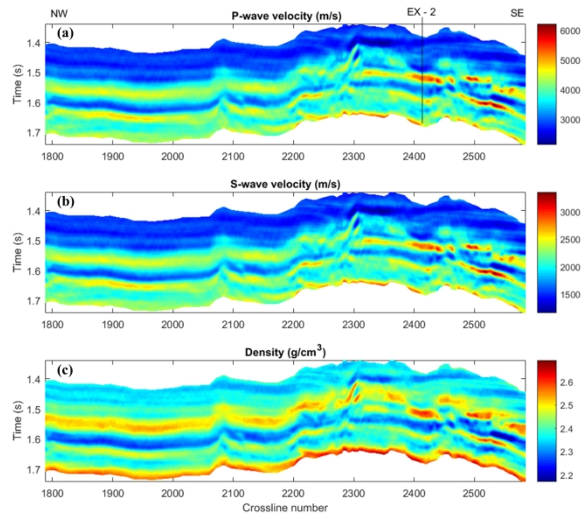

Figure 9: 2-D inversion of inline for (a) P-wave velocity, (b) S-wave velocity, and (c) density.

338x190mm (300 x 300 DPI)

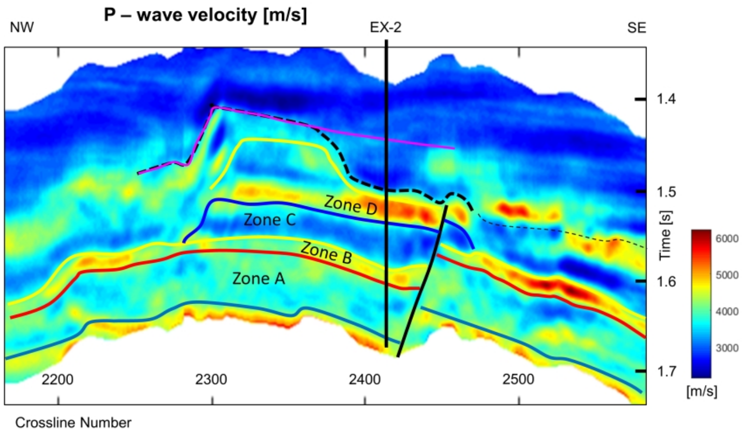

Figure 10: Zoom of 2-D inversion of inline for P-wave velocity. Horizons A – E delineate the reservoir zone boundaries, dividing zones A - D (adapted from Rankey et al. 2019).

338x190mm (300 x 300 DPI)

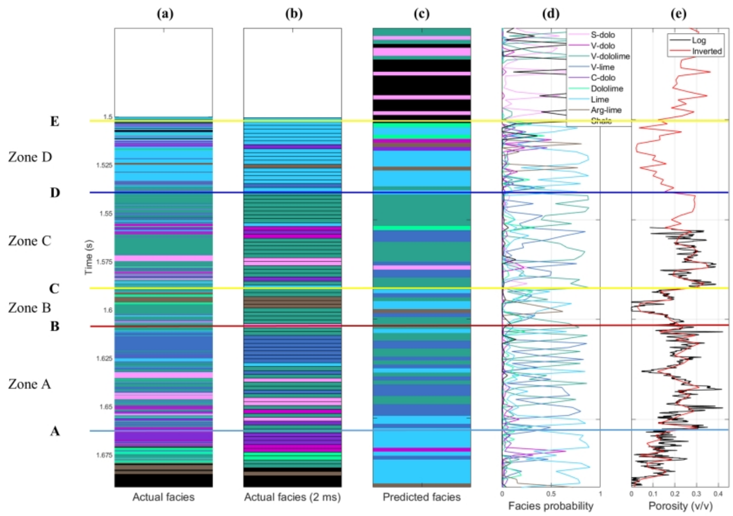

Figure 11: Inversion results from well data. (a) Actual facies from core in time domain. (b) Actual facies from core, upscaled to seismic sampling rate of 2 ms. (c) Predicted facies resulting from 1-D inversion at well location with upscaled (2 ms) elastic and density well log data as inputs. (d) Probabilities of individual facies. (e) Predicted porosity from 1-D inversion at well location (red) using upscaled (2 ms) elastic and density well log data as inputs.

338x190mm (300 x 300 DPI)

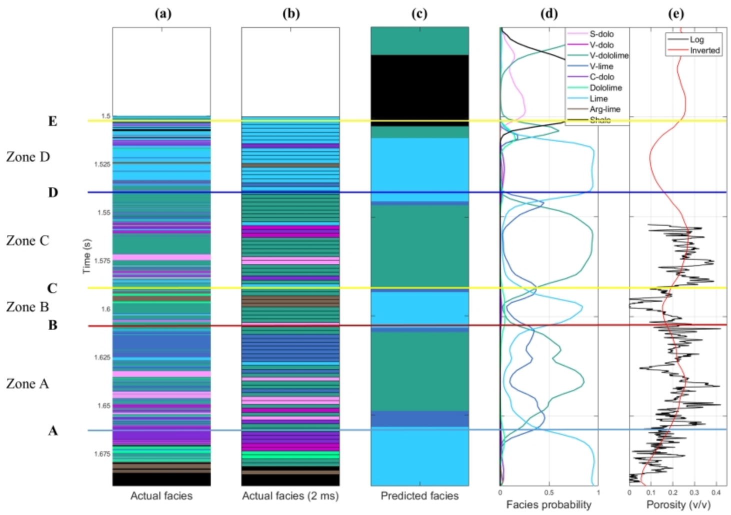

Figure 12: Inversion results from seismic data at well EX-2 trace. (a) Actual facies from core in time domain. (b) Actual facies from core, upscaled to seismic sampling rate of 2 ms. (c) Predicted facies resulting from 1-D inversion at well location with extracted seismic trace as input. (d) Probabilities of individual facies. (e) Predicted porosity from 1-D inversion at well location (red) using extracted seismic trace as input.

338x190mm (300 x 300 DPI)

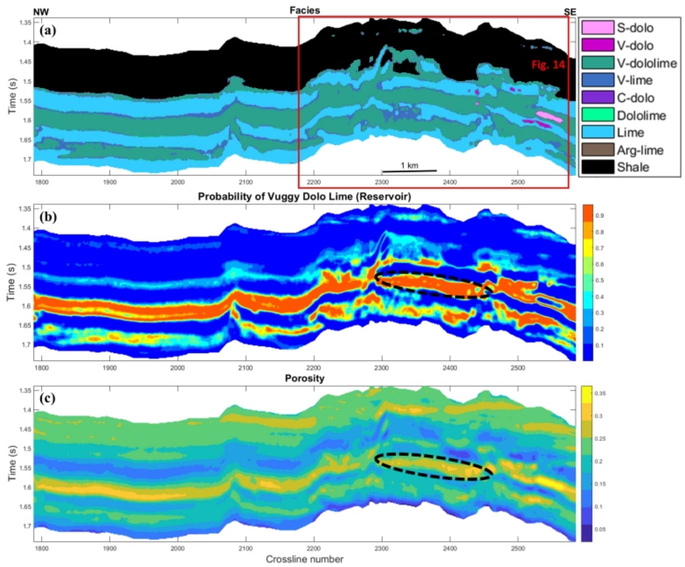

Figure 13: 2-D inversion of extracted inline that crosses EX-2 well location. (a) Facies results displayed as the maximum value. The red box is displayed in Figure 14 with an interpretation framework. (b) probability of vuggy dolomitized limestone, a preferential reservoir facies. An elongated reservoir body is encircled by a black dashed line. (c) Inversion result for porosity. The reservoir body in (b) shows increasing porosity values toward southeast. The well EX-2 is located at trace 2410.

338x190mm (300 x 300 DPI)

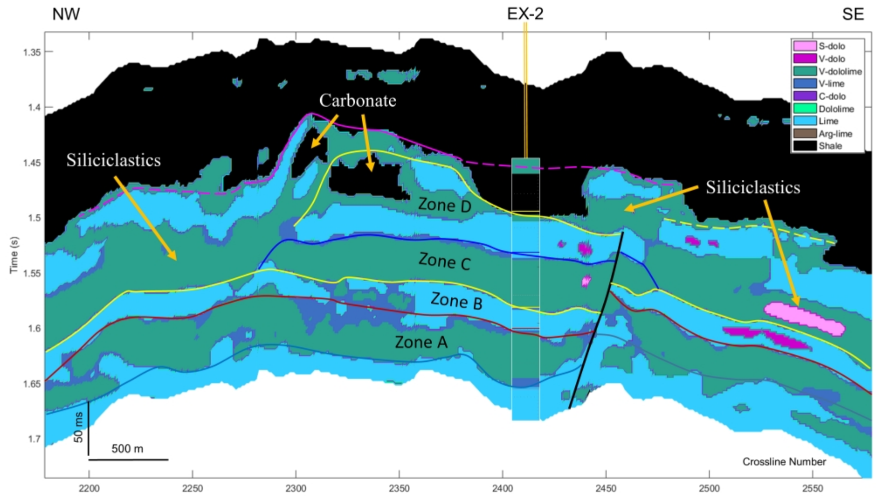

Figure 14: Interpreted 2-D facies inversion of EX carbonate platform, showing reservoir horizons and reference well EX-2 (orange). At the well location, the 1-D facies inversion result from the extracted seismic trace is shown for comparison.

338x190mm (300 x 300 DPI)

	Bulk modulus (GPa)	Shear Modulus (Gpa)	Density (g/cm³)	Average Dolomite (%)
Sucrosic dolomite	53	35	2.65	79
Vuggy dolomite	66	32	2.74	74
Vuggy dolomitized limestone	76	19	2.8	35
Vuggy limestone	72	20	2.77	11
Crystalline dolomite	56	29	2.67	77
Dolomitized limestone	43	19	2.6	25
Limestone	53	22	2.65	13
Argillaceous limestone	38	18	2.5	19
Shale	29	13	2.4	32

Table 1: Bulk and shear moduli and density of the mineral phase from rock physics modeling and mineralogical data from calcimetry showing average dolomite content for each facies.

DATA AND MATERIALS AVAILABILITY

Data associated with this research are confidential and cannot be released.

DOI:10.1190/geo2020-0351.1